ASTM INTERNATIONAL

Geotechnical Testing Journal

Joanna Butlanska,[1] Marcos Arroyo,[2] Sara Amoroso,[3] and Antonio Gens[2]

DOI: 10.1520/GTJ20170370

Marchetti Flat Dilatometer Tests in a Virtual Calibration Chamber

Geotechnical Testing Journal

doi:10.1520/GTJ20170370 available online at www.astm.org

Joanna Butlanska,[1] Marcos Arroyo,[2] Sara Amoroso,[3] and Antonio Gens[2]

Marchetti Flat Dilatometer Tests in a Virtual Calibration Chamber

Reference

Butlanska, J., Arroyo, M., Amoroso, S., and Gens, A., "Marchetti Flat Dilatometer Tests in a Virtual Calibration Chamber," *Geotechnical Testing Journal* https://doi.org/10.1520/GTJ20170370. ISSN 0149-6115

ABSTRACT

Calibration chambers are frequently used to verify, adapt, or both verify and adapt empirical relations between different state variables and in situ test results. Virtual calibration chambers (VCC) built with 3D discrete element models may be used to extend and partially substitute costly physical testing series. VCC are used here to explore the mechanics of flat dilatometer penetration and expansion. Results obtained for a simulation of physical tests in Ticino sand are presented. Blade tip resistance during penetration is in good agreement with the experiments. A piston-like design is used for the blade so that larger displacements may be applied than it is possible with a membrane. Initial piston pressures in the expansion curves are very low, strongly affected by the scaled-up grain sizes. Despite that difficulty, expansion curves may be easily interpreted to recover dilatometer moduli E_D close to those observed in the physical experiments. Particle-scale examination of the results allows a firmer understanding of the current limitations and future potential of the technique.

Keywords

flat dilatometer, discrete element method, numerical modeling, penetration resistance, calibration chamber, stiffness

Manuscript received October 14, 2017; accepted for publication May 11, 2018; published online July 5, 2018.

[1] Department of Civil and Environmental Engineering, Geosciences Division, UPC, Jordi Girona 1-3, Modul D2, 08034, Spain (Corresponding author), e-mail: joanna.butlanska@upc.edu, https://orcid.org/0000-0003-3447-4346

[2] Department of Civil and Environmental Engineering, Geosciences Division, UPC, Jordi Girona 1-3, Modul D2, 08034, Spain, https://orcid.org/0000-0001-9384-9107 (M.A.), https://orcid.org/0000-0001-7588-7054 (A.G.)

[3] Istituto Nazionale di Geofisica e Vulcanologia, Viale Crispi 43, L'Aquila 67100, Italy, https://orcid.org/0000-0001-5835-079X

Introduction

In 1975, Silvano Marchetti (Marchetti 1975) introduced a simple spade-like soil-testing apparatus called the flat dilatometer (DMT). The DMT is now accepted as one of the main in situ tests (Schnaid 2009) with a large field of applications (Failmezger and Anderson 2006, Marchetti, Monaco, and Viana Da Fonseca 2015), such as site profiling, soil parameter identification, evaluation of liquefaction potential, pile design, etc.

In standard testing procedures (ISO 22476-11, *International Standard. Geotechnical Investigation and Testing—Field Testing—Part 11: Flat Dilatometer Test*; ASTM D6635-15, *Standard Test Method for Performing the Flat Plate Dilatometer*; and EN 1997-2:2007, *Eurocode 7: Geotechnical Design—Part 2: Ground Investigation and Testing*) the DMT blade is inserted in the soil and stopped at regular intervals to expand the membrane. Two pressures are determined: the contact pressure, p_0, when the membrane is

flush with the blade, and p_1, pressure when the membrane center has displaced 1.10 mm into the soil. The electromechanical principle underlying standard DMT measurements offers robustness and repeatability, but with just two pressure values, relatively little information is obtained from the test. Modified dilatometers, usually built for research purposes (Campanella and Robertson 1991, Fretti, Lo Presti, and Salgado 1992, Akbar and Clarke 2001, Stetson, Benoit, and Carter 2003, Colcott and Lehane 2012), are able to register the complete load-displacement curve of the membrane. Frequently these research dilatometers also acquire other measurements, like pore pressure on the blade or resistance to DMT blade penetration, q_d.

The interpretation and use of DMT results has generally followed an empirical approach, mostly based on well-documented correlations with other test results and calibration chamber (CC) testing. For granular soils, this approach is costly. Correlation with laboratory test results (e.g., Tanaka and Tanaka 1998) requires good quality samples, typically obtained by in situ freezing. Physical CC suitable for a DMT are large and expensive to build and operate. As a consequence, relatively few CC DMT campaigns have been performed to date (Baldi et al. 1986, Motan and Khan 1988, Smith 1993, Bellotti et al. 1997, Lee et al. 2011).

In principle, numerical modeling of the DMT offers an alternative avenue to advance test understanding. In practice, realistic numerical modeling of the DMT is quite challenging, because the penetration phase involves large strains and displacements. Moreover, the problem is clearly 3D, as evidenced by the stress and strain fields after undrained insertion that were obtained using the strain path method by Huang (1989) and Finno (1993). Unfortunately, the strain path method cannot go much further, as it cannot represent drained conditions or membrane expansion.

When a Lagrangian finite element method (FEM) formulation is applied, mesh distortion strongly limits the penetration that can be achieved. This limitation affects several studies (Luo and Xu 2006, Balachowski 2006, Colcott and Lehane 2012) that are also somewhat limited by different geometrical simplifications employed to examine the problem in 2D. An enhanced 3D FEM, such as that used by Kouretzis et al. (2015), is potentially more versatile; nevertheless, the results presented by those authors—a relation between the horizontal stress index K_D and the overconsolidation ratio OCR close to previous empirical correlations—were still restricted to undrained DMT insertion.

The discrete element method (DEM) is able to quantitatively reproduce the behavior of granular materials in most conditions (O'Sullivan 2011). In DEM, material description is made at the grain scale and typically requires far less tunable parameters than what are necessary in realistic continuum models of granular soils. DEM simulation results can be examined at various levels of resolution (macro-, meso-, and microlevel) and described using both continuum-inspired and discrete variables (Butlanska et al. 2014). DEM is also well adapted to problems involving large displacements, such as DMT insertion. Xu and Frost (2015) presented a pioneering 2D DEM analysis of DMT insertion and expansion. The study was qualitative and there was no intention to compare results with experimental data.

3D DEM is necessary to obtain more realistic results. For the similar problem of cone penetration test (CPT) insertion, virtual calibration chambers (VCC) have been built using 3D DEM models showing good quantitative agreement with experimental results (Arroyo et al. 2011, Ciantia et al. 2016, Holmen, Olovsson, and Børvik 2017). The VCC approach is applied here for the first time to the more complex case of the DMT. In what follows, we first describe the numerical model employed and the physical CC tests that are used for comparison. We later present the relevant macroscale results obtained for both penetration and expansion phases. Mesoscale and microscale results are then examined to highlight some model responses and modeling challenges. Finally, some conclusions are drawn.

Model Description

MODEL GEOMETRY

The model aims to reproduce some DMT performed in a physical CC at Istituto Sperimentale Modelli e Strutture in Bergamo and Ente Nazionale per l'Energia Elettrica in Milan (Baldi et al. 1986, Jamiolkowski, Lo Presti, and Manassero 2003). The models were built adapting a procedure previously used to simulate CPT (Arroyo et al. 2011, Butlanska et al. 2014). The PFC3D code (Itasca Consulting Group 2008) is used for all simulations.

The DMT device is built using rigid walls, maintaining the main dimensions of the physical instrument. However, instead of a flexible membrane, a rigid piston with diameter of 60 mm was introduced. This alternative design has previously been implemented in several research DMT (Akbar and Clarke 2001, Colcott and Lehane 2012). Work with those apparatus shows that the piston solution allows larger displacements in the expansion phase. It does also show that, in their common displacement range, piston DMT and standard DMT obtain very similar results. From the numerical viewpoint the piston solution is advantageous, because it can simply be modeled with a series of rigid walls.

A schematic view of the DMT device and VCC employed is shown in **Fig. 1**. The chamber is also built with wall elements that can be either fixed or servo-controlled to maintain a specified boundary stress. The VCC has the same diameter as in the experiment (see **Table 1**), but it is shorter to reduce the computational cost. In the horizontal section only half a chamber is modeled, introducing a vertical wall aligned with the symmetry axis of the penetrating blade. Arroyo et al. (2013) showed that, for CPT penetration, this introduced little error in comparison to

FIG. 1
Schematic view of DMT and VCC.

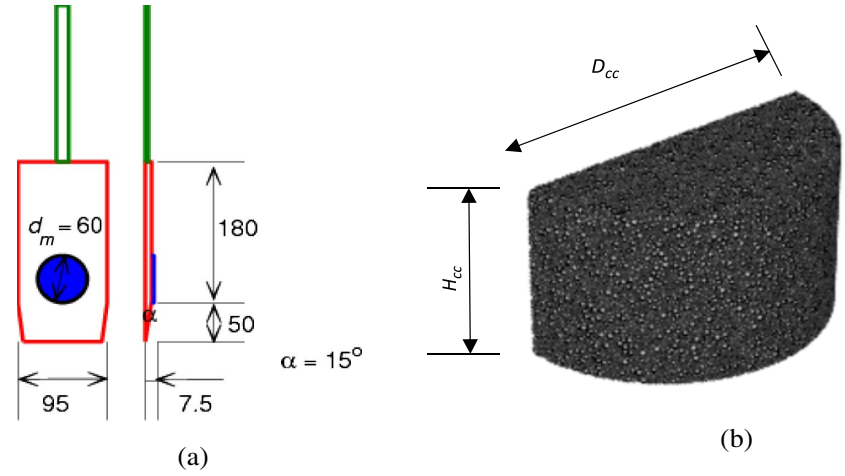

TABLE 1 Comparative geometrical characteristics of experimental and simulated CC.

Variable	Unit	Symbol	Experiment	DEM
Chamber diameter	mm	D_{CC}	1,200	1,200
Chamber height	mm	H_{CC}	1,500	700
Membrane diameter	mm	d_m	60	60
Particle mean size	mm	d_{50}	0.53	15.9
Piston/particle ratio	–	$r_p = d_m/d_{50}$	113	3.77
Number of particles	–	Np	$\sim 2 \times 10^{10}$	~138,800

whole chamber results. During DMT penetration, the problem has indeed such a plane of symmetry, although during expansion that symmetry is lost in the physical model, because there is a membrane only in one side of the DMT blade. A similar half chamber model was employed by Kouretzis et al. (2015).

DISCRETE MATERIAL MODEL

The target DMT experiments were performed in a physical chamber filled with Ticino sand. Ticino sand is a well-known reference sand (Jamiolkowski, Lo Presti, and Manassero 2003) whose grain size distribution is illustrated in **Fig. 2**.

There are too many sand grains in the physical experiment (see **Table 1**) to map each one of them into a discrete element. In the approach followed here (Arroyo et al. 2011, Ciantia et al. 2016), a computationally manageable number of elements is attained by scaling particle size. The scaling factor applied is 30, and the grain size distribution of the discrete elements is thus a shifted version of that of Ticino sand without fines (see **Fig. 2**).

After scaling, the size of the discrete elements is on the gravel range. Because the DMT dimensions are not scaled, the ratio of piston diameter to particle mean size in the model, r_p, is much smaller than the equivalent ratio (membrane diameter to particle

FIG. 2
Grain size distribution curves.

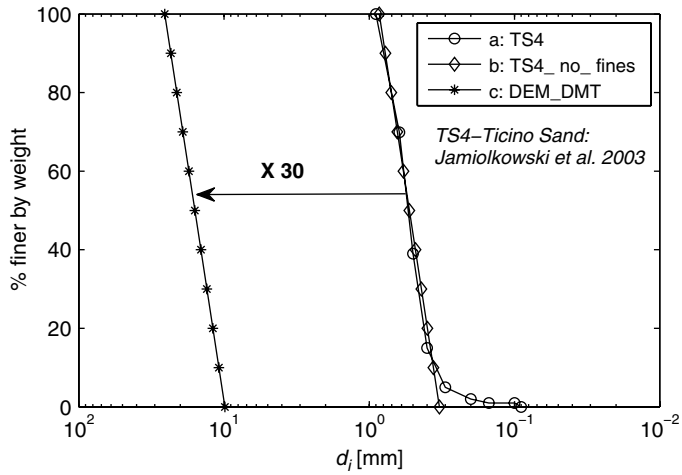

mean size) in the reference experiment (see **Table 1**). This model feature imposes some constraints on the results, which are later discussed.

The contact law is linear elastoplastic. The contacts support no tension and slide when the ratio of tangential and normal forces is above the friction coefficient, given by tan ($\Phi\mu$). Macroscopic stiffness is insensitive to the particle scaling factor (Gabrieli, Cola, and Calvetti 2009) when normal and tangential contact stiffness, k_N and k_S, are described by the following:

$$k_N = 2K_{eff}\frac{D_1 D_2}{D_1 + D_2} \tag{1}$$

$$k_S = \alpha k_N$$

where D_1 and D_2 are the diameters of contacting particles. K_{eff}, α, and φ_μ are material parameters, evaluated as explained later. To achieve rapid convergence, the simulations also employ a small amount of non-viscous local damping, δ. The gravity is switched off. The discrete elements employed are spherical, but particle rotations are prevented, to roughly mimic the increased strength due to non-spherical particle shapes (Ting et al. 1989). Because of its mineralogy (siliceous), the crushability of Ticino sand is quite small; taking profit of that particle breakage was neglected in this analysis.

The contact model parameters (see **Table 2**) are the same applied in previous simulations of CPT in Ticino sand (Arroyo et al. 2011, Butlanska, Arroyo, and Gens 2010b). As explained there, they were obtained by matching the response of a single drained triaxial test and then verified using other triaxial results.

TESTING PROGRAM

Four DMT tests from the experimental series were selected as targets for simulation. The initial and boundary conditions of these tests are reported in **Table 3**. The nomenclature for CC boundary conditions (Jamiolkowski, Lo Presti, and Manassero 2003) denotes the radial stress control as BC1 and radial fixed wall as BC3. In direct correspondence with the laboratory setup, the horizontal top wall was fixed and the bottom wall servo-controlled to maintain constant vertical stress.

The particles were placed in the VCC using the radius expansion method. A numerical servo-controlled mechanism was implemented to attain the target stress state and density. The numerical specimen was compressed by controlled movement of all walls (top, bottom, outer, and wall enforcing model symmetry). The initial conditions attained before DMT testing are listed in **Table 3**. In some cases, there was a small difference between the values attained in the simulation and those in the reference experiment. For these cases, two values are indicated in the table, with the values in parentheses corresponding to the physical test.

TABLE 2 Model parameters used in DEM simulations.

Parameter	Unit	Symbol	Value
Particle friction coefficient	–	tan($\Phi\mu$)	0.35
Coefficient K_{eff}	MPa	K_{eff}	300
Local damping	–	δ	0.05
Particle density	kg/m^3	ρ_g	2690
Stiffness ratio	–	α	0.25

TABLE 3 Initial conditions for the DMT CC tests.

Test ID	σ_v kPa	σ_h kPa	e –	D_R %	OCR –	BC –
T100	111	84.4	0.655 (*0.649*)	77.7 (*79.4*)	2.8	1
T101	111	61	0.656 (*0.650*)	77.4 (*79.2*)	1.5	1
T271	112	47	0.656	77.4	1	1
T109	112 (*113*)	47	0.656 (*0.649*)	77.4 (*79.5*)	1	3

Note: σ_v = total vertical stress, σ_h = total horizontal stress, e = void ratio, D_R = relative density, OCR = overconsolidation ratio.

Macroscale Results

PENETRATION STAGE

The rigid DMT was pushed in the discrete assembly at a rate of 10 cm/s. This advance rate is five times faster than that applied in the experiments but remains within the quasi-static regime in which inertial effects are negligible (Butlanska, Arroyo, and Gens 2010a; Quezada et al. 2014; Janda and Ooi 2016).

During DMT, blade position, blade penetration resistance q_d, and other relevant quantities, such as blade-particle contacts, were continuously registered. Blade penetration resistance was calculated as follows:

$$q_d = \frac{\sum_i F_{iz}}{A_b} \tag{2}$$

where $\sum F_{iz}$ represents the sum of the vertical forces acting on the blade walls, and A_b is the cross-sectional area of the blade.

Blade resistance penetration curves for the physical and virtual CC are plotted together in **Fig. 3** against normalized chamber depth. It can be observed that simulations compare quite well to the experiments. End effects affect the penetration curves. In the laboratory, curve pushing halts for DMT expansion are visible as resistance drops. The large oscillations visible in the simulated curves are a consequence of the scaled-up size of the particles (Arroyo et al. 2011, Butlanska, Arroyo, and Gens 2013) and can be considered numerical noise.

Numerical noise can be filtered from the raw penetration curves by fitting them with the following expression (Arroyo et al. 2011):

$$q_{d,trend}(m_z) = q_{d,ss}(1 - e^{-bm_z}) \tag{3}$$

FIG. 3 DMT blade resistance in Ticino Sand: simulation and laboratory results for (a) T100 (BC1 OCR = 2.8), (b) T101 (BC1 OCR = 1.5), (c) T271 (BC1 OCR = 1) and (d) T109 (BC3 OCR = 1).

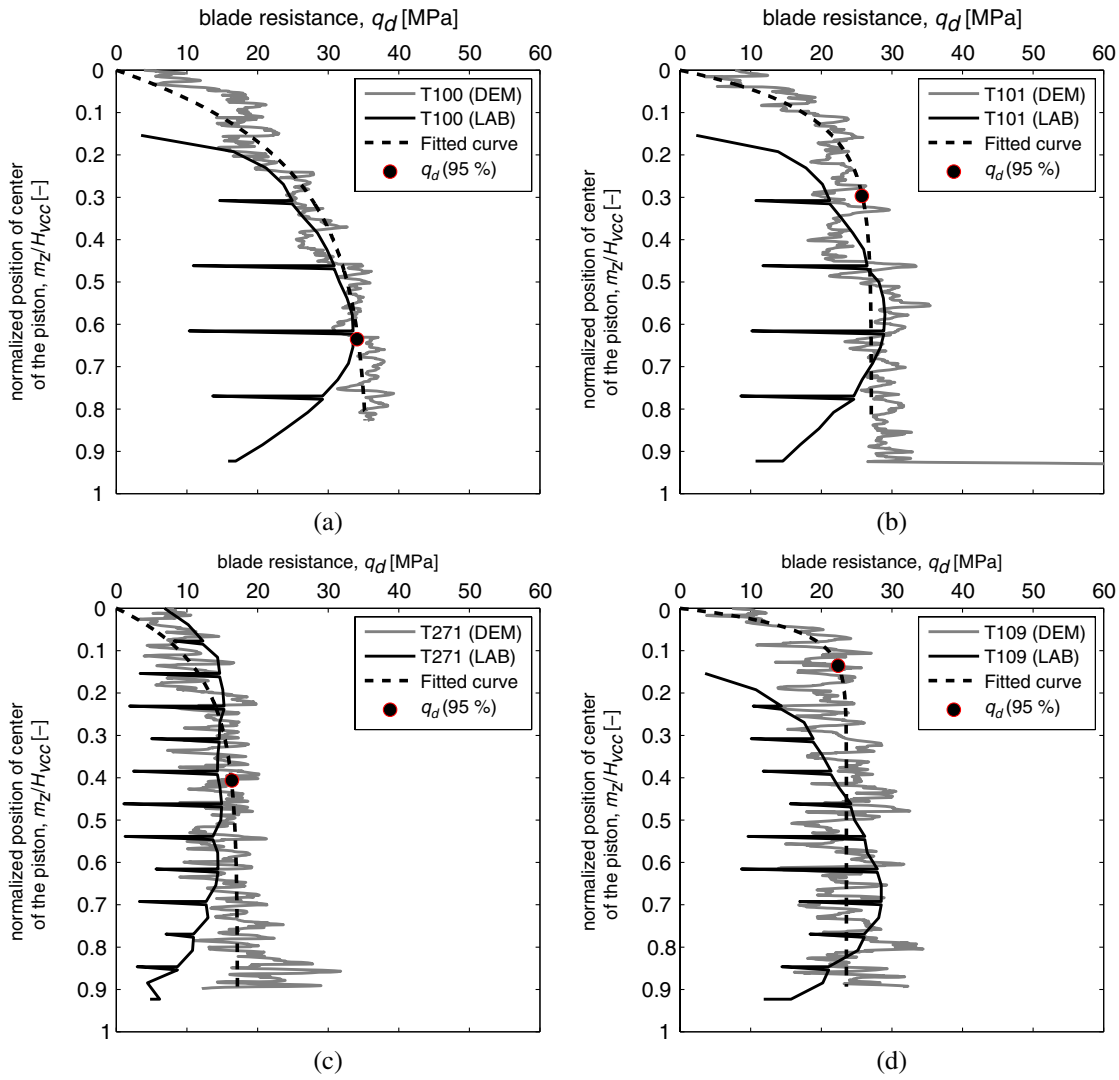

where $q_{d,trend}$ (MPa) is the blade resistance, m_z is the piston center position, and $q_{d,ss}$ and b are the fitting parameters. Parameter $q_{d,ss}$ (MPa) gives the asymptotic or steady state value of blade resistance, whereas parameter b (1/m) is inversely related to the depth at which the steady state is attained. For instance, calling h_{SS}, the position of piston center at which 95 % of the steady state value is reached, then:

$$h_{ss} \approx \frac{3}{b} \tag{4}$$

The relevant values were extracted and are listed in **Table 4**. The comparison between the experimental q_{d_LAB} (measured in the center of CC) and the steady state value extracted from numerical results is quite good.

EXPANSION STAGE

The DMT employed in the physical CC experiments was a conventional one, and only p_0 and p_1 values were recorded in the membrane expansion phase. There was some variability in the results for a given CC test, and the values reported in **Table 5** correspond to those measured at mid-chamber height.

In the VCC, the blade penetration was stopped at mid-height, and the specimen was brought to equilibrium. Afterwards the piston was pushed horizontally inside the assembly at 5 cm/s. Piston pressure p was computed as the sum of normal forces $\sum F_{in}$ divided by piston area A_P as follows:

$$p = \frac{\sum F_{in}}{A_P} \tag{5}$$

TABLE 4 DMT penetration: laboratory and simulation results.

Test ID	q_{d_LAB} MPa	$q_{d,ss}$ (Eq 3) MPa	q_{d_LAB} / $q_{d,ss}$ –	b (Eq 3) 1/m	q_d (95%) MPa	h_{ss} m	h_{ss}/H_{cc} –
T100	32.68	35.891	0.91	−7	34.09	0.428	0.635
T101	28.8	27.093	1.06	−15	25.74	0.200	0.297
T271	13.68	17.164	0.80	−11	16.31	0.273	0.405
T109	26.17	23.559	1.11	−33	22.38	0.091	0.135

TABLE 5 Simulation and laboratory results from DMT expansion.

	Lab			DEM	
Test ID	p_0 kPa	p_1 kPa	p_0/p_1 –	t_0 mm	t_1 mm
T100	577.8	1612	0.358	1.3	2.8
T101	388.7	1613	0.241	1.3	3.5
T271	455.3	1520	0.299	1.2	2.8
	394	1214	0.324	0.1	0.8

FIG. 4 Simulated DMT expansion curves: (a) T100 (BC1 OCR = 2.8), (b) T101 (BC1 OCR = 1.5), (c) T271 (BC1 OCR = 1), and (d) T109 (BC3 OCR = 1).

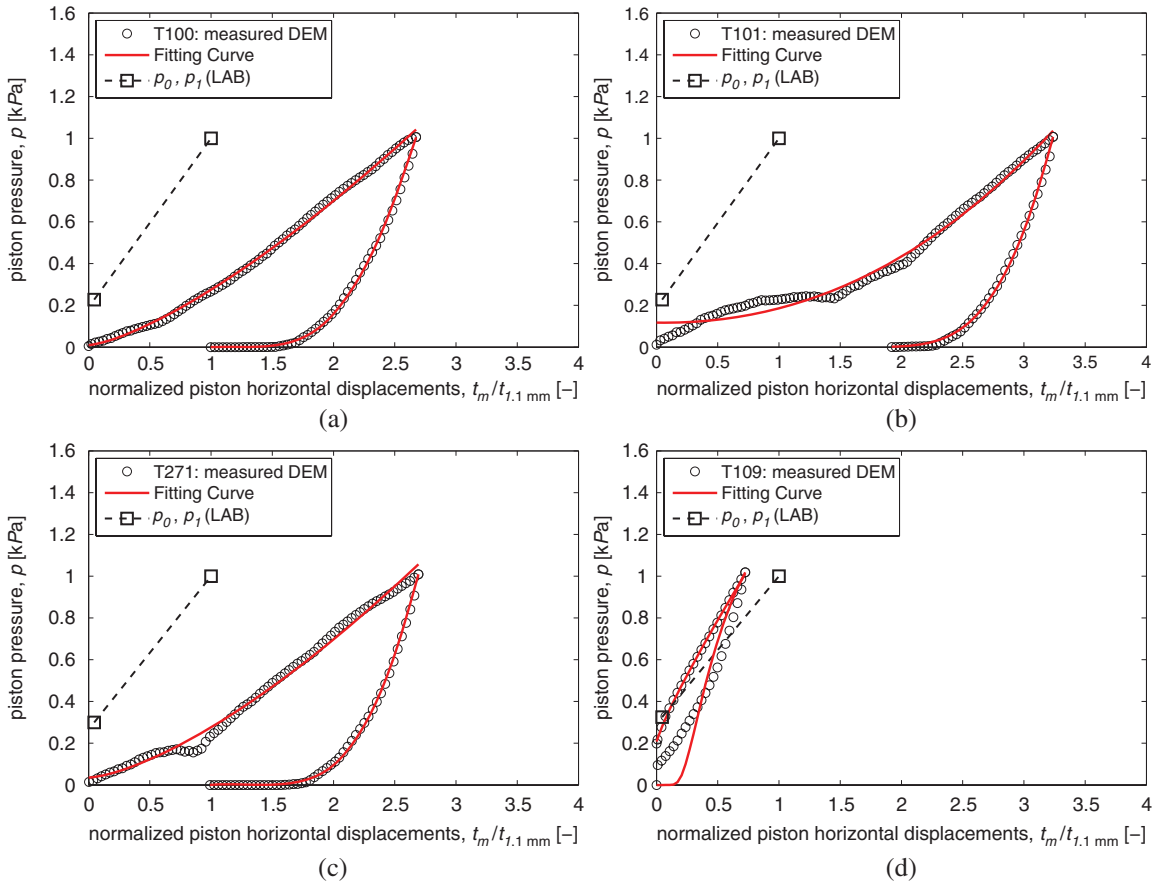

After some trials, it appeared that the relatively large ratio of particle to piston size required displacements larger than the standard value (1.1 mm) to mobilize significant resistance. Expansion was then continued until the experimental p_1 reading (see **Table 5**) was attained. Afterwards, unloading proceeded.

The numerical piston loading–unloading curves for the different tests are shown in **Fig. 4**. The pressure axis is normalized by *p1*, and the displacement axis is normalized by the standard displacement at p_1 (1.1 mm), namely $t_{1.1\ mm}$. Piston displacements corresponding to the experimental p_0 and p_1 values (respectively denoted as t_0 and t_1) are listed in **Table 5**. The experimental points corresponding to p_0 and p_1 are also represented in **Fig. 4**.

Numerical tests performed in BC1 conditions show an almost negligible piston pressure before expansion, followed by a marked stiffening behavior during expansion. A piston displacement of around three times the standard value was required to attain the target pressure. On the other hand, the numerical test performed under BC3 conditions showed a significant initial pressure and a linear stiffer response. All the unloading curves evidence a significant plastic residual displacement at the piston face.

The very low initial piston pressures observed in the numerical tests are due to the relatively large particle/piston size. Similar observations of very low p_0 values are reported for tests on gravelly layers (Monaco, Totani, and Amoroso 2015). Indeed, such low pressures were one of the original reasons—the other being physical damage to membranes—why gravelly soils were deemed unsuitable for DMT testing (Marchetti and Crapps 1981). On the other hand, the curve shape obtained for the BC3 test is quite similar to that observed in similar experiments with research dilatometers (e.g., Bellotti et al. 1997).

Because of the relatively large particle size the piston expansion curves show also some irregularities, even if at a much lesser scale than the penetration curves. To ease interpretation the pressure-displacement curves were also smoothed by curve fitting to the raw data points. Two different formulations were employed. For the expansion curves (i.e., piston loading) a power function was used as follows:

$$p = At^B + C \tag{6}$$

where A, B, and C are fitting parameters, t is the piston displacement, and p is the piston pressure. For the unloading part of the pressure-displacement curve, the expression used was as follows:

$$p = p_u \cdot \frac{\mathrm{erfc}\left(\frac{\alpha}{t}\right)}{\mathrm{erfc}\left(\frac{\alpha}{t_u}\right)} \tag{7}$$

where α is a fitting parameter and (t_u, p_u) is a starting point in unloading curve. The complementary error function *erfc(x)* is defined as follows:

$$\mathrm{erfc}(x) = 1 - \mathrm{erf}(x) = 1 - \frac{2}{\sqrt{\pi}} \int_0^x e^{-s^2}\,\mathrm{ds} \tag{8}$$

where *erf(x)* is the error function, i.e., the integral of a Gaussian distribution with 0 mean and a variance of ½, and s is a dummy variable.

The fitting procedure described was implemented in MATLAB (MathWorks, Natick, MA). The curves obtained are shown in **Fig. 4** for loading and unloading stages. The fitting parameters are listed in **Table 6**. The fitting is very good, with

TABLE 6 Expansion stage: fitting parameters for loading and unloading curves.

	Loading Part			Unloading Part
Test ID	A	B	C	α
T100	375.65	1.38	14.70	4.218
T101	89.12	2.21	189.56	6.357
T271	319.01	1.45	53.15	4.775
T109	1,186.16	0.99	252.52	0.359

TABLE 7 Dilatometer moduli evaluated from laboratory and simulation results.

Test ID	E_D MPa	E_{D_DEM} MPa	E_D /E_{D_DEM} –	E_{UR_DEM} MPa	(E_{UR_DEM} / E_{D_DEM}) –
T100	35.9	29.3	1.23	116.6	3.97
T101	42.5	34.3	1.24	130.5	3.80
T271	36.9	28.1	1.31	137.2	4.88
T109	28.5	45.0	0.63	–	–

TABLE 8 Macroscopic effects of scaling factor.

Test ID	$q_{d,ss}$ (Eq 3) MPa	STD MPa	t_0 mm	t_1 mm	A –	B –	C –	α –	E_{D_DEM} MPa	E_{UR_DEM} MPa
$T271_{S=30}$	17.164	4.6	1.2	2.8	319	1.45	53.14	4.8	28.1	137.2
$T271_{S=40}$	22.62	6.5	2.7	9.1	125	1.11	78.7	19.9	6.7	66.7
$T271_{S=50}$	18.64	7.5	4.4	8.2	38.3	1.78	−68.9	18	13.1	74.5

TABLE 9 Microscopic effects of scaling factor.

Test ID	D_{50}, mm	N_{tot}	B_A/A_{d50}	$N_{c1,max}$	$N_{c1,ave}$	d_m/D_{50}	$N_{c2,\ max}$	$N_{c2,\ ave}$
$T271_{S=30}$	17.6	139E3	70.3	81	58	3.77	13	10
$T271_{S=40}$	22.6	59E3	42.6	41	27	2.8	8	4
$T271_{S=50}$	26.5	30E3	31.0	30	16	2.26	4	2

FIG. 5 Effects of particle scaling: (a) piston-particle contacts during penetration, (b) horizontal stress acting on piston during penetration stage, (c) piston-particle contacts during piston expansion, and (d) fitted piston load-unload curves.

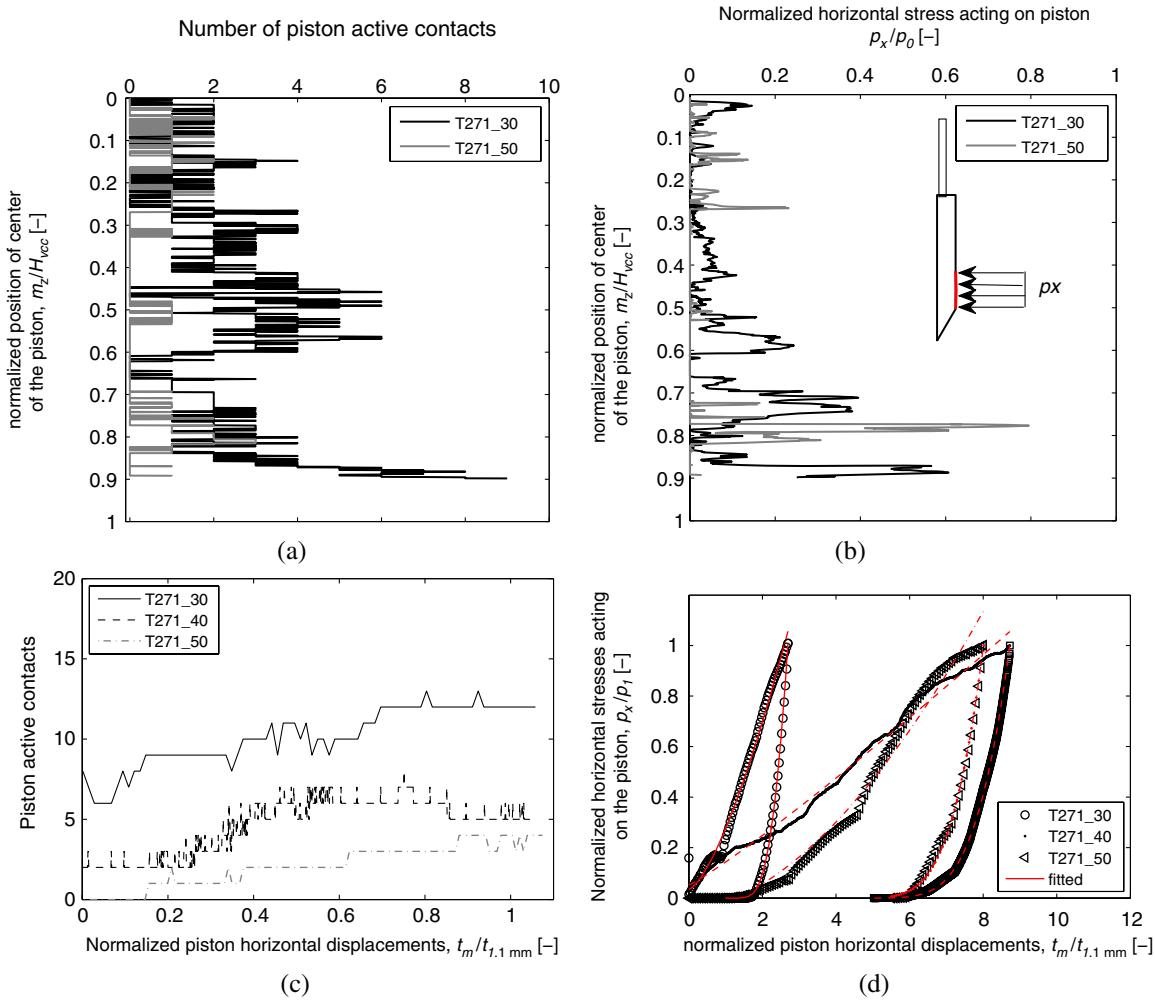

FIG. 6 Tip penetration resistance and piston horizontal stresses during penetration: (a) T271 (BC1 OCR = 1) and (b) T109 (BC3 OCR = 1).

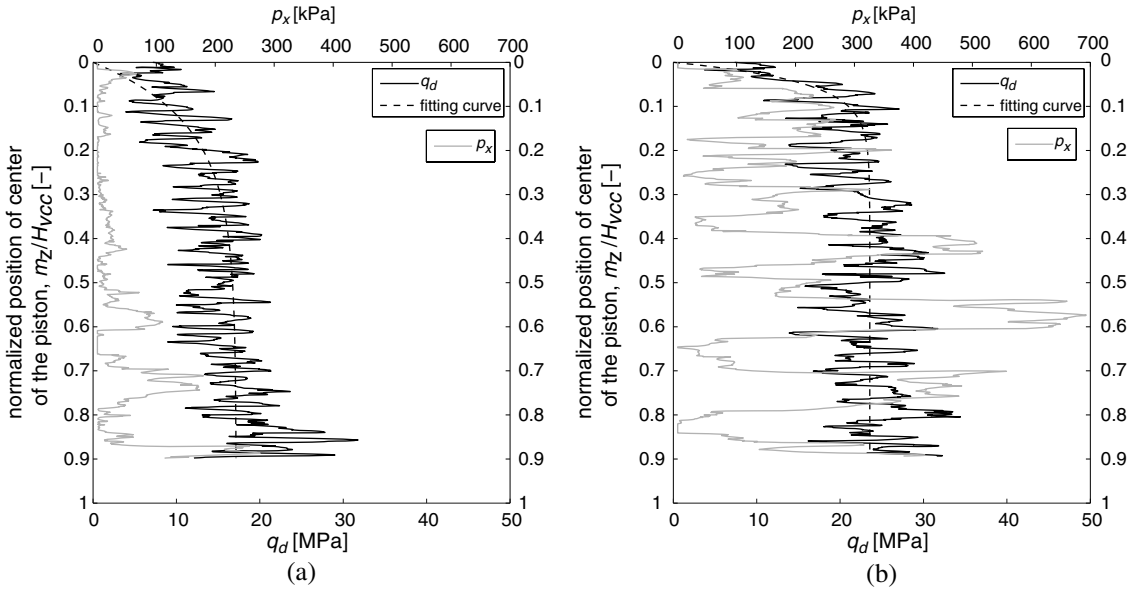

regression coefficient R^2 above 0.98 in all cases—except the unloading branch of T109, where the fitting is poorer both quantitatively ($R^2 < 0.9$) and qualitatively (the fitted curve appears to have the opposite curvature than that showed by the data).

DILATOMETER MODULUS

Following Marchetti (1980), three calculated results are obtained from each DMT expansion test: the material index, I_D, the horizontal stress index, K_D, and the dilatometer modulus E_D, as follows:

$$I_D = \frac{p_i - p_0}{p_0 - u_0} \tag{9}$$

$$K_D = \frac{p_i - p_0}{\sigma'_{v0}} \tag{10}$$

$$E_D = 34.7(p_i - p_0) \tag{11}$$

Where u_o and σ'_{v0} are, respectively, the pore pressure and vertical effective stress before testing.

The dilatometer modulus E_D formula is based on the analogy of the test with the case of a rigid wall, with a circular hole supporting an elastic half-space (Marchetti 1980). From the analytical solution for that case, it follows that:

$$E_D = \frac{E}{(1-\nu^2)} = \frac{2D}{\pi}\frac{(p_1 - p_0)}{t} \tag{12}$$

The standard formula is obtained by substituting $t = 1.1$ mm and $D = 60$ mm. For a nonlinear expansion curve, this elastic analogy can be simply generalized to the following:

$$E_D = \frac{2D}{\pi}\frac{dp}{dt}\bigg|_{t=1.1} \tag{13}$$

Using the analytical expression proposed above to fit the numerical results, it follows that:

$$E_{D\_DEM} = \frac{2D}{\pi} AB\, t_1^{(B-1)} \tag{14}$$

The same procedure may be applied to the unloading branch, to obtain a tangent unloading modulus as follows:

$$E_{UR\_DEM} = p_1 \frac{2D}{\pi}\frac{2\alpha}{\sqrt{\pi}}\frac{1}{erfc\left(\frac{\alpha}{t_1}\right)}\frac{e^{-\left(\frac{\alpha}{t_1}\right)^2}}{t_1^2} \tag{15}$$

The moduli thus computed are gathered in **Table 7**. For the tests performed under the BC1 boundary condition, the experimental E_D is somewhat above that obtained from the simulation. The opposite happens for the test performed under BC3 conditions, which shows a stiffer response in simulation. There were no unloading branches in the physical CC tests selected for the comparison; however, Fretti, Lo Presti, and Salgado (1992) measured ratios $E_{UR}/E_D \approx 7$ for Ticino sand for other BC1 tests in similar conditions ($\sigma_v \approx 100$ kPa, $OCR \approx 1$-3). It then appears that the simulations underestimate experimental unloading stiffness by a larger factor than loading stiffness. This may be related to the known limitations of the simple linear particle contact model employed here to represent stiffness at different strain levels (Otsubo et al. 2017).

FIG. 7 Vertical and radial stress changes around the DMT probe: (a) T271 (BC1 $OCR = 1$) (σ_z), (b) T109 (BC3 $OCR = 1$) (σ_z), (c) T271 (BC1 $OCR = 1$) (σ_r), and (d) T109 (BC3 $OCR = 1$) (σ_r).

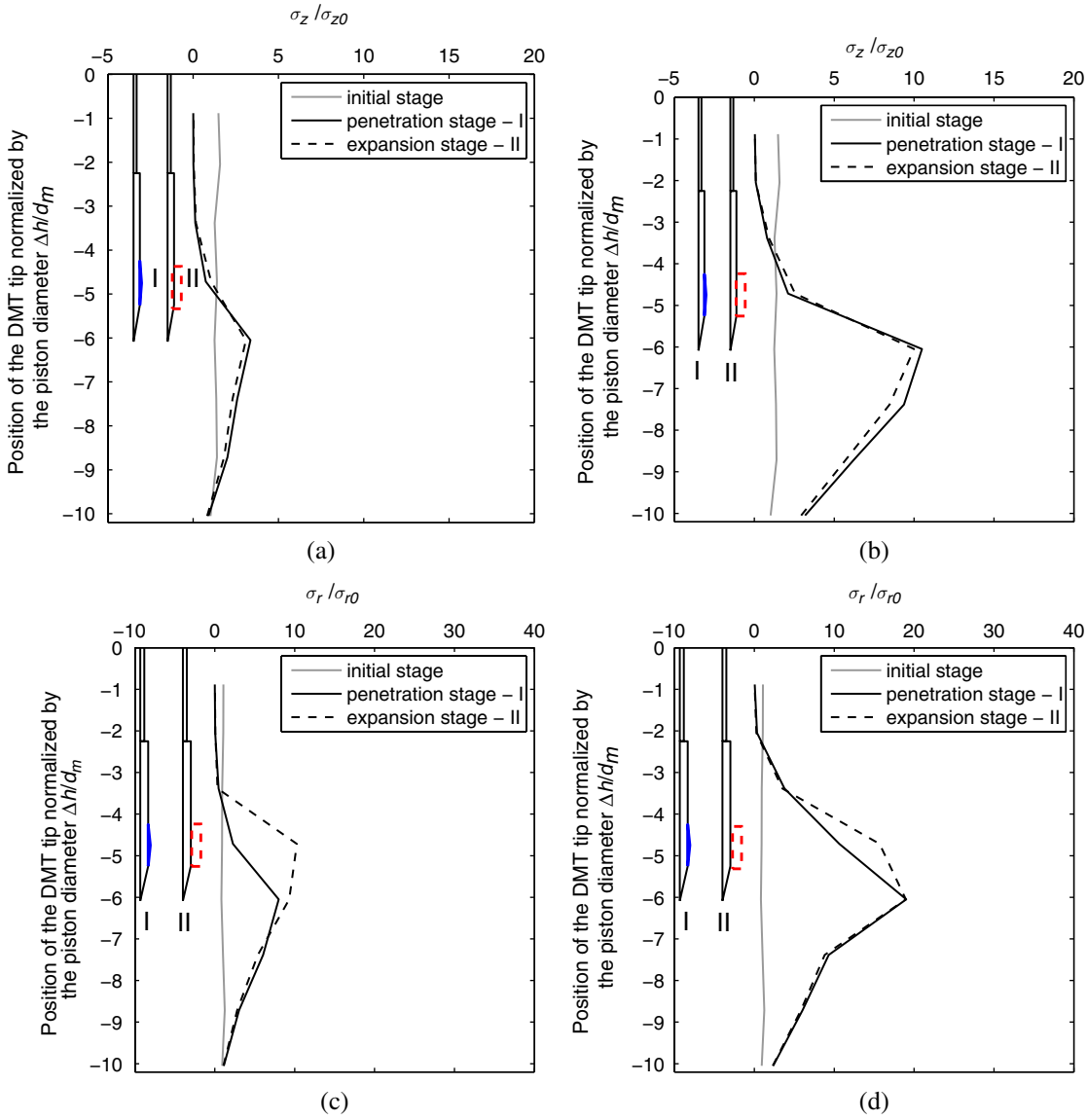

Sensitivity Analyses

EFFECT OF PARTICLE SCALING FACTOR

A significant constraint on the model, imposed by computational limitations, is the need to scale up grain size. The scaling factor, S, applied to the Ticino sand grain size in the test described earlier, was 30 (see **Fig. 2**). To better understand the implications of this on model results, two repeats of Test T271 were made with larger scaling factors of 40 and 50.

The main macroscopic results of this test series are collected in **Table 8**, whereas some particle-scale quantities of interest are presented in **Table 9**. Amongst the latter we include: particle mean size, D_{50}; total number of particles, N_{tot}; ratio of blade side area ($B_A = 171$ cm^2) and mean particle projected area $A_{d50} = (\pi/4)(D_{50})^2$; maximum ($N_{c1,max}$) and average ($N_{c1,ave}$) number of blade to particle force-carrying contacts during penetration; the ratio of piston diameter ($d_m = 60$ mm) to mean grain size, D_{50}; and the maximum ($N_{c2,max}$) and average ($N_{c2,ave}$) number of piston to particle force-carrying contacts during penetration. In addition to this tabulated data, some selected results of this series are illustrated in **Fig. 5**.

There is no clear effect of the particle scaling factor in the steady state blade resistance during penetration ($q_{d,ss}$, see **Table 8**), while the regression mean error (STD, see **Table 8**) shows a small increase with particle size. This is in agreement with previous studies of CPT (Butlanska, Arroyo, and Gens 2013). Such

FIG. 8 Binary plot of cumulative particle displacement around the DMT probe during penetration: (a) front view T271 (BC1 *OCR* = 1), (b) front view T109 (BC3 *OCR* = 1), (c) side view T271 (BC1 *OCR* = 1), and (d) side view T109 (BC3 *OCR* = 1). White = downwards motion and black = upwards motion.

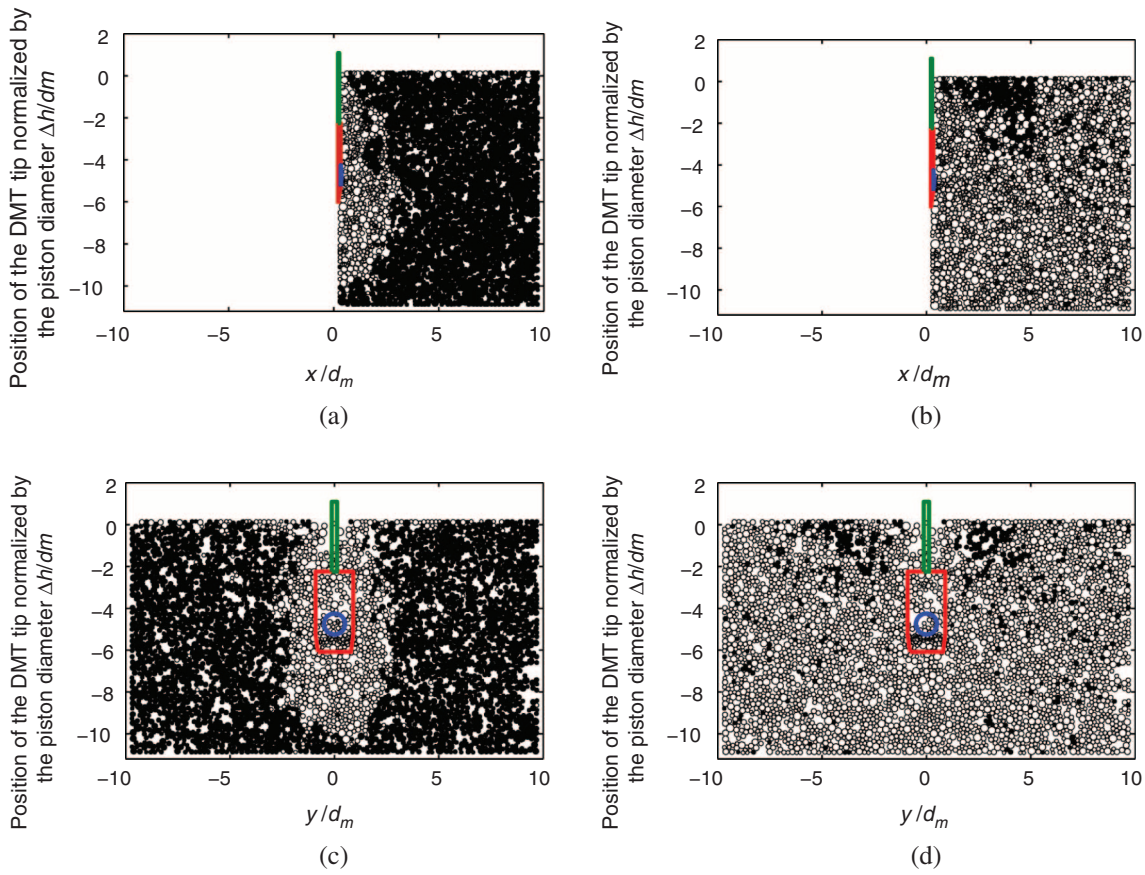

insensitivity may be related to the relatively large blade side area (see B_A/A_{d50} values in **Table 9**). Even if blade-particle contact numbers (see $N_{c1,max}$ and $N_{c1,ave}$ in **Table 9**) diminish significantly with increased scaling, the mean value for the largest scaling factor $S = 50$ is still 16.

The piston area is only one sixth of the blade side area. The numbers of piston-particle contacts during penetration ($N_{c2,max}$ and $N_{c2,ave}$, see **Table 9**) are reduced in a similar proportion. Particle to piston contact numbers (see **Fig. 5a**) show that for the largest scaling factor ($S = 50$), there are numerous times during penetration in which the piston has only a single particle in contact or even no contact at all. For the lower scaling factor ($S = 30$), the situation may not be so extreme, but the number of contacts is still small. The small contact numbers explain the very low piston pressures that are recorded during penetration (see **Fig. 5b**), with few instances in which the pressure raises above 20 % of the experimental p_0 value.

The piston displacements required to attain pressures p_0 and p_1 (i.e. t_0 and t_1) strongly increase with particle size: for instance, t_0 goes from 7 % to 25 % of D_{50}. Piston-particle contacts during the expansion stage are shown in **Fig. 5c** and the corresponding load-unload fitted curves in **Fig. 5d**. It appears that the piston needs to engage with at least 12 particles to mobilize stiffness close to that of the granular mass. This suggests a micromechanically based criterion to stop piston advance, which may be used on its own in numerical analysis (i.e., without the need to resort to a previously known experimental value of p_1).

RADIAL BOUNDARY EFFECT

One of the most significant differences observed in the previous section is that between simulations performed under constant lateral stress condition (BC1) and those performed under a fixed radial boundary condition (BC3). Comparing the results from Tests T271 (BC1) and T109 (BC3), it appears that changing the boundary condition results in much increased penetration resistances (see **Table 4**) and dilatometer modulus E_D (see **Table 7**). It is also clear that in BC3 conditions, piston stress during penetration has a higher average and larger oscillations (see **Fig. 6**).

The effects may be explained by observing the stress changes induced by the DMT in a vertical line close to the chamber axis. **Fig. 7** plots particle stress averages during penetration and at maximum expansion. These were obtained by means of measurement

FIG. 9 Force patterns around the DMT probe during penetration: (a) front view T271 (BC1 OCR = 1), (b) front view T109 (BC3 OCR = 1), (c) side view T271 (BC1 OCR = 1), and (d) side view T109 (BC3 OCR = 1).

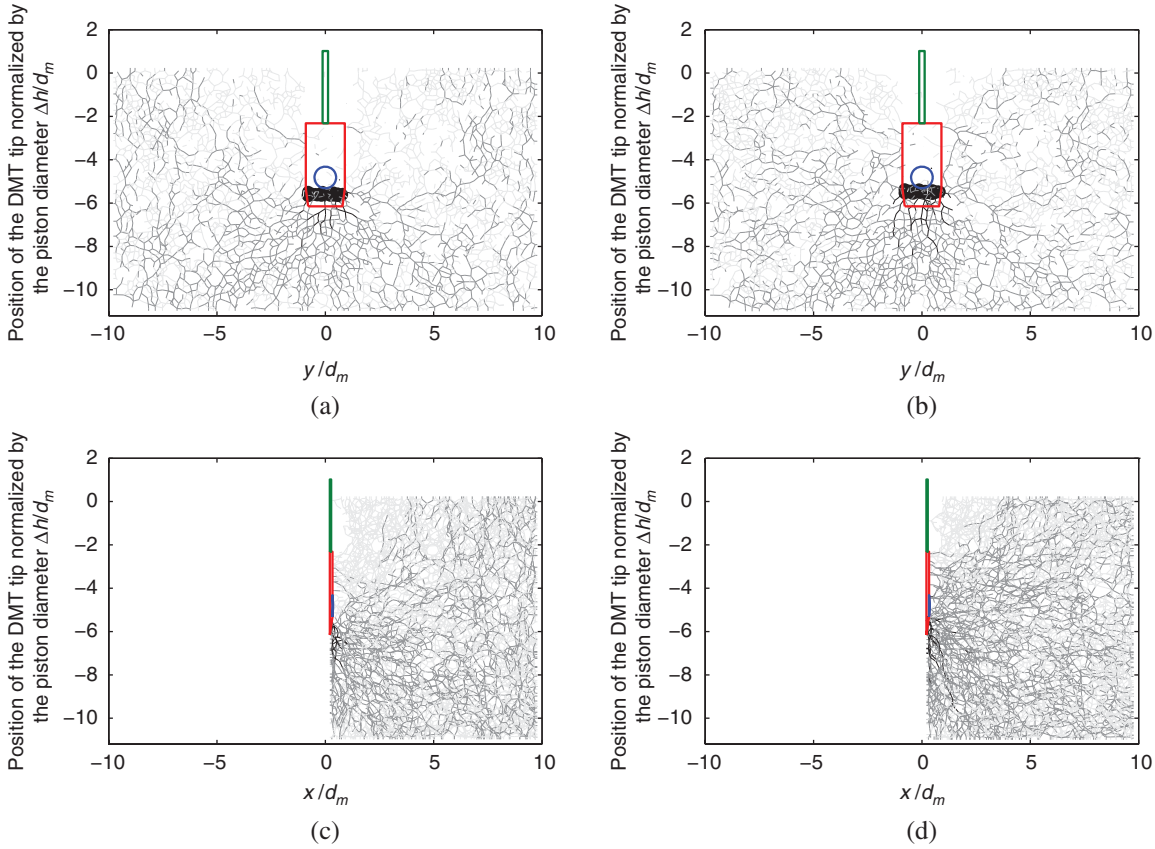

FIG. 10 (a,b) Tip penetration resistance and piston horizontal stresses and (c,d) snapshots of force distributions on a vertical section during penetration. Test T271 (BC1 OCR = 1).

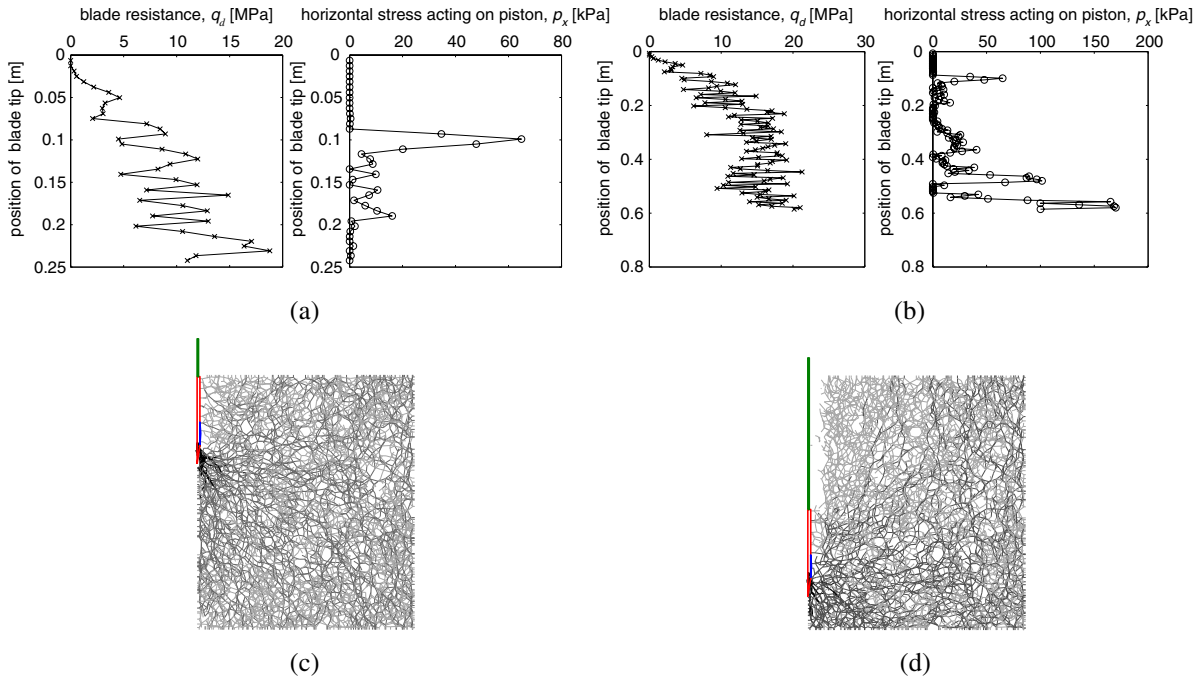

spheres of a 5-cm radius with centers located at $r = 6.5$ cm from the blade and opposite to its in-plane symmetry axis.

Upon penetration, a bulb of highly increased stress is induced below the instrument tip, followed by a significant stress reduction alongside the shaft, behind the blade. These stress changes are qualitatively similar to those induced by CPT penetration (Yang et al. 2014, Butlanska et al. 2014). The rigid boundary results in a larger increase in stress below the blade, and in a smaller and slower fall in stress behind the blade. Piston expansion then causes a far more significant radial stress increase for the BC1 case.

Microscale kinematics around the penetrating probe are also strongly influenced by the chamber boundary conditions (see **Fig. 8**). As may be expected, DMT blade penetration is accompanied by a downward motion of the particles surrounding the probe. However, the volume involved in this downward motion depends very much on the boundary condition. For the BC1 case, only a central section, between 3 and 4 piston diameters wide around the blade, follows its motion. For the BC3 case, almost the whole chamber is displaced downwards alongside the blade.

FORCE PATTERN

Contact force plots are useful to explore force transmission across the system at the particle scale. Such patterns have finer resolution than what is obtained when plotting stress averages. In what follows, we present some contact force plots, in which force vectors are represented in planar *xz*- and *yz*-projection along a vertical section containing the axis. In the force graphs following, line thickness is proportional to the magnitude of the normal force; extreme forces, (i.e., those exceeding the average value +5 standard deviations), are illustrated in black; large (above average but not extreme) are shown in dark gray; and small (below average) are marked in light gray.

For instance, the stress changes in **Fig. 7** express the different granular force transmission patterns that are visible at the particle scale (see **Fig. 9**). A shadow of negligible force transmission is created behind the blade tip during penetration. This shadow zone does include the piston for the BC1 case, but not for the BC3 case. It is clear that the horizontal rigid boundary is able to sustain much larger horizontal forces. As a consequence, the force network appears more horizontally directed, and its disruption by blade insertion around the shaft does not reach the piston depth.

Force patterns can also be employed to further understand the oscillatory nature of the piston forces during the penetration process. When an instrument like the DMT is advanced into a granular mass, a forced granular flow around the instrument takes place. As it happens in other instances of granular flow (Zuriguel et al. 2017), this flow-around has an intermittent cyclic nature, and sudden reconfigurations of the force patterns take place during penetration. Interestingly, the frequency of tip resistance oscillation is higher than that of piston stress changes (see **Fig. 10**).

The force patterns shown also in **Fig. 10** suggest an explanation: piston loads appear to respond to an avalanching mechanism, in which an active wedge falls in the nearly empty space that is left behind the blade. The spatial extent and timing of this mechanism may have been affected by a lack of gravity in the model, an aspect currently under investigation.

As a final example, the force pattern during piston expansion is now considered. During piston expansion, the force pattern created during penetration changes radically (see **Fig. 11**).

Initially the strong force chain pattern is directed subvertically, with the strong force chains emanating from the blade tip and low force region at the piston face (see **Fig. 11a**). As the piston is pushed into the chamber, sub-horizontal strong force chains, emanating from the piston face, become more important.

FIG. 11 Contact force developing around the blade during different stages of piston expansion (t_m) for T271 (BC1 $OCR = 1$): (a) $t_m = 0$ mm, (b) $t_m = 2.8$ mm, and (c) $t_m = 31.8$ mm.

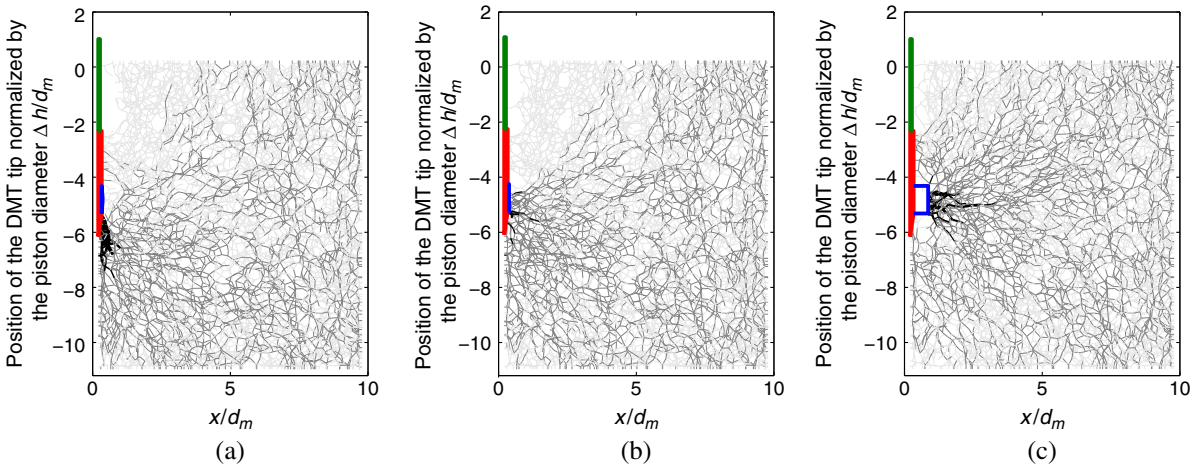

FIG. 12

Distribution of contact forces at the end of expansion stage (at $t_m = t_1$): (a) T100 (BC1 OCR = 2.8), (b) T101 (BC1 OCR = 1.5), (c) T271 (BC1 OCR = 1), and (d) T109 (BC3 OCR = 1).

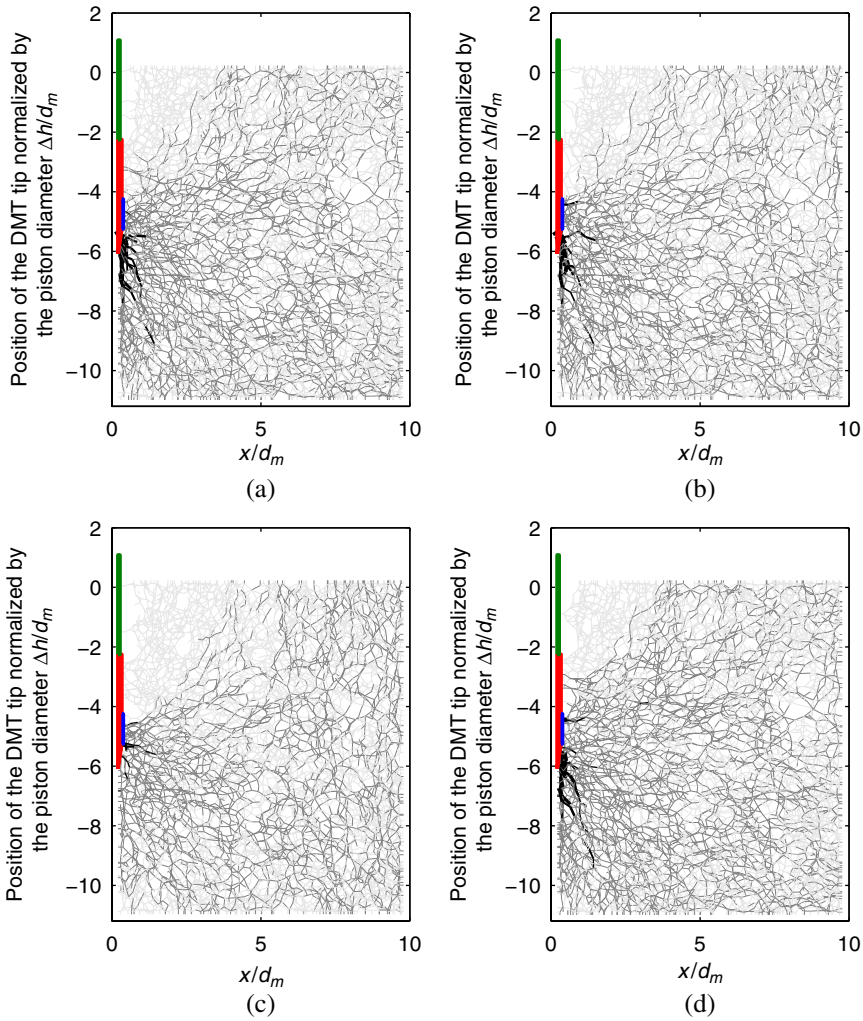

By the time p_1 is attained (see **Fig. 11b**), the prevalence of sub-horizontal strong force chains is clear, although the pattern still shows some vertical bias towards the blade tip. If the pushing is further continued (see **Fig. 11c**), that vertical bias practically disappears, and the strong force chain network shows a nearly symmetrical distribution around the face. Interestingly, both increased *OCR* and the change to a rigid boundary condition seem to attenuate the phenomenon (see **Fig. 12**). As an aside, it is worth noting that the effect of the half-chamber wall appears rather small even during this nonsymmetric expansion phase.

The force pattern changes just discussed imply that principal stress rotations in front of the DMT would be very significant, going beyond those induced already by penetration. A corollary (Jiang, Harris, and Zhu 2007) is that continuum-based approaches that aim to model DMT insertion and expansion should be able to correctly represent material response under principal stress rotation.

Conclusions

Despite its increasingly important role as a site investigation tool, DMT simulation procedures have offered very limited results to date. This is a consequence of the difficulties associated with a realistic representation of a truly 3D insertion test. This research set out to explore if 3D DEM models offer a mean to study the mechanics of DMT insertion and expansion in granular soils. From the results presented, it can be concluded that, despite some limitations, VCC may significantly contribute in this area. In particular, it has been shown that the numerical models:

1. were able to reproduce well the experimentally observed blade penetration resistances; and
2. resulted in a tangent dilatometer modulus evaluated at the p_1 pressure level, ED_DEM, within 30 % of the experimental values.

The simulation technique employed imposes some constraints. In particular, it is necessary to scale up particle size to reduce computational load. This conduces a particle to instrument size ratio, which is similar to that of gravelly soils. The number of particles in contact with the piston is affected by scaling, and this results in very low p_0 values. Piston displacements required to attain p_1 pressures are also higher than in the physical experiments. However, a micromechanical criterion (number of active contacts with the piston of 10-12) may be used as an alternative criterion to identify the p_1 stress level, and, consequently, to extract a dilatometer modulus from simulated expansion curves.

ACKNOWLEDGMENTS

The research was supported by the Spanish Ministry of Economy through Grant (BIA2014-59467-R). The support provided by the EU-funded GEO-RAMP RISE project (H2020-645665-GEO-RAMP) is also acknowledged.

References

Akbar, A. and Clarke, B. G., 2001, "A Flat Dilatometer to Operate in Glacial Tills," *Geotech. Test. J.*, Vol. 24, No. 1, pp. 51–60, https://doi.org/10.1520/GTJ11281J

Arroyo, M., Butlanska, J., Gens, A., Calvetti, F., and Jamiolkowski, M., 2011, "Cone Penetration Test in a Virtual Calibration Chamber," *Géotechnique*, Vol. 61, No. 6, pp. 525–531, https://doi.org/10.1680/geot.9.P.067

Arroyo, M., Butlanska, J., Gens, A., and O'sullivan, C., 2013, "The Effect of Radial Walls on CPT in a DEM-Based Virtual Calibration Chamber," presented at the *Third International Symposium on Computational Geomechanics*, Krakow, Poland, Aug. 21–23, 2013, International Centre for Computational Engineering, Rhodes, Greece.

ASTM D6635-15, 2015, *Standard Test Method for Performing the Flat Plate Dilatometer*, ASTM International, West Conshohocken, PA, www.astm.org

Balachowski, L., 2006, "Numerical Modelling of DMT Test in Calibration Chamber," *Studia Geotechnica et Mechanica*, Vol. 28, Nos. 2–4, pp. 21–30.

Baldi, G., Bellotti, R., Ghionna, V., Jamiolkowski, M., Marchetti, S., and Pasqualini, E., 1986, "Flat Dilatometer Tests in Calibration Chambers," *Use of In Situ Tests in Geotechnical Engineering*, American Society of Civil Engineers, Reston, VA, pp. 431–446.

Bellotti, R., Benoît, J., Fretti, C., and Jamiolkowski, M., 1997, "Stiffness of Toyoura Sand from Dilatometer Tests," *J. Geotech. Geoenviron. Eng.*, Vol. 123, No. 9, pp. 836–846, https://doi.org/10.1061/(ASCE)1090-0241(1997)123:9(836)

Butlanska, J., Arroyo, M., Gens, A., and O'sullivan, C., 2014, "Multi-Scale Analysis of Cone Penetration Test (CPT) in a Virtual Calibration Chamber," *Can. Geotech. J.*, Vol. 51, No. 1, pp. 51–66, https://doi.org/10.1139/cgj-2012-0476

Butlanska, J., Arroyo, M., and Gens, A., 2013, "Steady State of Solid-Grain Interfaces during Simulated CPT," *Studia Geotechnica et Mechanica*, Vol. 35, No. 4, pp. 13–22, https://doi.org/10.2478/sgem-2013-0034

Butlanska, J., Arroyo, M., and Gens, A., 2010a, "Size Effects on a Virtual Calibration Chamber," presented at the *Seventh European Conference on Numerical Methods in Geotechnical Engineering-Numerical Methods in Geotechnical Engineering*, Trondheim, Norway, June 2–4, 2010, CRC Press, Boca Raton, FL, pp. 225–230.

Butlanska, J., Arroyo, M., and Gens, A., 2010b, "Virtual Calibration Chamber CPT Tests on Ticino Sand," presented at the *Second International Symposium on Cone Penetration Testing*, Huntington Beach, CA, May 9–11, 2010, Gregg Drilling and Testing, Inc., Signal Hill, CA, pp. 217–224.

Campanella, R. G. and Robertson, P. K., 1991, "Use and Interpretation of a Research Dilatometer," *Can. Geotech. J.*, Vol. 28, No. 1, pp. 113–126, https://doi.org/10.1139/t91-012

Ciantia, M. O., Arroyo, M., Butlanska, J., and Gens, A., 2016, "DEM Modelling of Cone Penetration Tests in a Double-Porosity Crushable Granular Material," *Comput. Geotech.*, Vol. 73, pp. 109–127, https://doi.org/10.1016/j.compgeo.2015.12.001

Colcott, R. and Lehane, B. M., 2012, "The Design, Development, and Application of a New DMT," *In Situ Geotechnical and Geophysical Site Characterization 4*, R. Q. Coutinho and P. W. Mayne, Eds., CRC Press, Boca Raton, FL, pp. 565–570.

EN 1997-2:2007, 2007, *Eurocode 7: Geotechnical Design—Part 2: Ground Investigation and Testing*, European Committee for Standardization, Brussels, Belgium, www.cen.eu

Failmezger, R. A. and Anderson, J. B., 2006, presented at *the Second International Conference on the Flat Dilatometer*, Washington, DC, April 2–5, 2006

Finno, R. J., 1993, "Analytical Interpretation of Dilatometer Penetration through Saturated Cohesive Soils," *Geotechnique*, Vol. 43, No. 2, pp. 241–254, https://doi.org/10.1680/geot.1993.43.2.241

Fretti, C., Lo Presti, D., and Salgado, R., 1992, "The Research Dilatometer: In Situ and Calibration Chamber Test Results," *Rivista Italiana di Geotecnica*, Vol. 26, No. 4, pp. 237–242.

Gabrieli, F., Cola, S., and Calvetti, F., 2009, "Use of an Up-Scaled DEM Model for Analysing the Behaviour of a Shallow Foundation on a Model Slope," *Geomech. Geoeng. Int. J.*, Vol. 4, No. 2, pp. 109–122, https://doi.org/10.1080/17486020902855688

Holmen, J. K., Olovsson, L., and Børvik, T., 2017, "Discrete Modeling of Low-Velocity Penetration in Sand," *Comput. Geotech.*, Vol. 86, pp. 21–32, https://doi.org/10.1016/j.compgeo.2016.12.021

Huang, A. B., 1989, "Strain-Path Analyses for Arbitrary Three-Dimensional Penetrometers," *Int. J. Numer. Anal. Meth. Geomech.*, Vol. 13, No. 5, pp. 551–564, https://doi.org/10.1002/nag.1610130507

ISO 22476-11, 2017, *International Standard. Geotechnical Investigation and Testing—Field Testing—Part 11: Flat Dilatometer Test*, International Organization for Standardization, Geneva, Switzerland, www.iso.org

Itasca Consulting Group, 2008, "PFC3D Version 4.1 Manual," Itasca Consulting Group, Inc., Minneapolis, MN.

Janda, A. and Ooi, J. Y., 2016, "DEM Modeling of Cone Penetration and Unconfined Compression in Cohesive Soil," *Powder Technol.*, Vol. 293, pp. 60–68, https://doi.org/10.1016/j.powtec.2015.05.034

Jamiolkowski, M., Lo Presti, D. C. F., and Manassero, M., 2003, "Evaluation of Relative Density and Shear Strength of Sands from CPT and DMT," presented at the *Symposium on Soil Behavior and Soft Ground Construction*, Cambridge, MA,

Oct. 5–6, 2001, American Society of Civil Engineers, Reston, VA, pp. 201–238.

Jiang, M. J., Harris, D., and Zhu, H. H., 2007, "Future Continuum Models for Granular Materials in Penetration Analyses," *Granular Matter*, Vol. 9, No. 1, pp. 97–108.

Kouretzis, G. P., Ansari, Y., Pineda, J., Kelly, R., and Sheng, D., 2015, "Numerical Evaluation of Clay Disturbance during Blade Penetration in the Flat Dilatometer Test," *Géotechnique Lett.*, Vol. 5, No. 3, pp. 91–95, https://doi.org/10.1680/jgele.15.00026

Lee, M. J., Choi, S. K., Kim, M. T., and Lee, W., 2011, "Effect of Stress History on CPT and DMT Results in Sand," *Eng. Geol.*, Vol. 117, Nos. 3–4, pp. 259–265, https://doi.org/10.1016/j.enggeo.2010.11.005

Luo, S. and Xu., C., 2006, "Numeric Modeling of the Flat Dilatometer Test," presented at the *GeoShanghai International Conference 2006*, Shanghai, China, June 6–8, 2006, American Society of Civil Engineers, Reston, VA, pp. 269–276.

Marchetti, S., 1975, "A New In Situ Test for the Measurement of Horizontal Soil Deformability," presented at the *Specialty Conference on In Situ Measurement of Soil Properties*, Raleigh, North Carolina, June 1–4, 1975, American Society of Civil Engineers, Reston, VA, pp. 255–259.

Marchetti, S., 1980, "In Situ Tests by Flat Dilatometer," *J. Geotech. Eng. Div.*, Vol. 106, No. 3, pp. 299–321.

Marchetti, S. and Crapps, D. K., 1981, *Flat Dilatometer Manual*, GPE Incorporated, Geotechnical Equipment, Gainesville, Fl, 95p.

Marchetti, S., Monaco, P., and Viana Da Fonseca, A., 2015, presented at the *Third International Conference on the Flat Dilatometer*, Rome, Italy, June 14–16, 2015, International Society of Soil Mechanics and Geotechnical Engineering, London, United Kingdom.

Monaco, P., Totani, G., and Amoroso, S., 2015, "SDMT-Based Analysis of the Liquefaction Phenomena Induced by the April 6, 2009 Earthquake at Ponte Rasarolo, L'Aquila (Italy)," presented at the *Third International Conference on the Flat Dilatometer*, Rome, Italy, June 14–16, 2015, International Society of Soil Mechanics and Geotechnical Engineering, London, United Kingdom, pp. 325–332.

Motan, E. S. and Khan, A. Q., 1988, "In-Situ Shear Modulus of Sands by a Flat-Plate Penetrometer: A Laboratory Study," *Geotech. Test. J.*, Vol. 11, No. 4, pp. 257–262, https://doi.org/10.1520/GTJ10656J

O'sullivan, C., 2011, *Particulate Discrete Element Modelling: A Geomechanics Perspective*, CRC Press, Boca Raton, FL, 576p.

Otsubo, M., O'sullivan, C., Hanley, K. J., and Sim, W. W., 2017, "The Influence of Particle Surface Roughness on Elastic Stiffness and Dynamic Response," *Géotechnique*, Vol. 67, No. 5, pp. 452–459, https://doi.org/10.1680/jgeot.16.P.050

Quezada, J. C., Breul, P., Saussine, G., and Radjai, F., 2014, "Penetration Test in Coarse Granular Material Using Contact Dynamics Method," *Comput. Geotech.*, Vol. 55, pp. 248–253, https://doi.org/10.1016/j.compgeo.2013.09.006

Schnaid, F., 2009, *In Situ Testing in Geomechanics: The Main Tests*, CRC Press, Boca Raton, FL, 352p.

Smith, M. G., 1993, "A Laboratory Study of the Marchetti Dilatometer," Ph.D. dissertation, University of Oxford, Oxford, England.

Stetson, K. P., Benoit, J., and Carter, M. J., 2003, "Design of an Instrumented Flat Dilatometer," *Geotech. Test. J.*, Vol. 26, No. 3, pp. 302–309, https://doi.org/10.1520/GTJ11303J

Tanaka, H. and Tanaka, M., 1998, "Characterization of Sandy Soils Using CPT and DMT," *Soils Found.*, Vol. 38, No. 3, pp. 55–65, https://doi.org/10.3208/sandf.38.3_55

Ting, J. M., Corkum, B. T., Kauffman, C. R., and Greco, C., 1989, "Discrete Numerical Model for Soil Mechanics," *J. Geotech. Eng.*, Vol. 115, No. 3, pp. 379–398, https://doi.org/10.1061/(ASCE)0733-9410(1989)115:3(379)

Xu, T. and Frost., J. D., 2015, "DEM Modeling of Insertion and Expansion during at Dilatometer Testing," presented at the *Third International Conference on the Flat Dilatometer*, Rome, Italy, June 14–16, 2015, International Society of Soil Mechanics and Geotechnical Engineering, London, United Kingdom, pp. 439–446.

Yang, Z. X., Jardine, R. J., Zhu, B. T., and Rimoy, S., 2014, "Stresses Developed around Displacement Piles Penetration in Sand," *J. Geotech. Geoenviron., Engineering*, Vol. 140, No. 3, 04013027, https://doi.org/10.1061/(ASCE)GT.1943-5606.0001022

Zuriguel, I., Janda, Á., Arévalo, R., Maza, D., and Garcimartín, Á., 2017, "Clogging and Unclogging of Many-Particle Systems Passing through a Bottleneck," *EPJ Web Conf.*, Vol. 140, pp. 1–8, https://doi.org/10.1051/epjconf/201714001002